Supplemental Document

Optics EXPRESS

Imaging device to measure the reflective and transmissive part of isotropic BSSRDF: supplement

MORGANE GERARDIN,[1,2,*] MATHIAS PAULIN,[2] AND ROMAIN PACANOWSKI[1]

[1] *Inria, France*
[2] *IRIT, University of Toulouse, CNRS, UT3, CIMI, Toulouse, France*
[*] *gerardin.morgane@gmail.com*

Supplement DOI: https://doi.org/10.6084/m9.figshare.27100609

Parent Article DOI: https://doi.org/10.1364/OE.538429

An imaging device to measure the reflective and transmissive part of isotropic BSSRDF: supplemental document

In this supplementary work we give details about the BSSxDF uncertainties computations. This includes both the absolute radiometric uncertainty related to the BSSxDF value ($\sigma_{f_{ssx}}$) and the geometric uncertainties related to the spatial and angular parameters of the measurements (σ_{θ_i}, σ_{ϕ_i}, σ_{θ_r}, σ_{ϕ_r}, $\sigma_{\mathbf{x_i}}$, $\sigma_{\mathbf{x_r}}$). We also provide details about the measurement process and more results obtained on two samples of interest.

1. UNCERTAINTY COMPUTATIONS

In this section, we describe the computations of the radiometric and geometric uncertainties. The radiometric uncertainties on both the incident flux and the observed radiance are computed by propagating the uncertainties of the different sources of errors involved. The geometric uncertainties arise from the calibration of the camera position with respect to the sample.

We use the notation σ_X to refer to the absolute uncertainty associated with the variable X. The relative uncertainty $u(X)$ is defined such as:

$$u(X) = \frac{\sigma_X}{X} \tag{S1}$$

A. Uncertainty evaluation

The evaluation of the uncertainty associated with a variable X depends on the type of measurement that is performed to establish such quantity. The random errors arising from multiple measurements of the same quantity may be distinguished from the systematic error that is intrinsic to the device used to measure the quantity.

Random errors: When the measurement of the same variable is performed N times, under the same conditions, there may be slight differences between the measurements. The resulting quantity that is actually considered as the real value is defined as the average of the N observations:

$$\bar{X} = \frac{1}{N}\sum_{k=1}^{N} X_k \tag{S2}$$

Statistically, and according to [1], the single observations X_k has the same absolute uncertainty that is defined as:

$$\sigma^2_{X_k} = \frac{1}{N-1}\sum_{j=1}^{N}(X_j - \bar{X})^2 \tag{S3}$$

The uncertainty associated with the mean quantity $\bar{X}$ then has the following expression:

$$\sigma^2_{\bar{X}} = \frac{\sigma^2_{X_k}}{N} = \frac{1}{N}\frac{1}{N-1}\sum_{j=1}^{N}(X_j - \bar{X})^2 \tag{S4}$$

Systematic errors: In a single measurement, the accuracy of the measuring device must be taken into account. When using a graduated tool (such as a ruler or a caliper), the measured quantity X lies within an interval $[a_-, a_+]$ of width equal to one graduation. The absolute uncertainty associated with X is then given by the formula (cf. [1], Sec. 4.3.7, Eq. 6):

$$\sigma^2_X = \frac{(a_+ - a_-)^2}{12} = \frac{(1\text{ graduation})^2}{12} \tag{S5}$$

For measurement devices, the manufacturer specifies that the quantity X is measured with a tolerance of t% plus a certain amount n of digit units. In this case, the measured X lies within an

interval of width $2a$ where $a = tX + n$. The absolute uncertainty induced by the measurement device is then given by (cf. [1], Sec. 4.3.7, Eq. 7):

$$\sigma_X^2 = \frac{tX + n}{3} \tag{S6}$$

Uncertainty propagation: The evaluation of the uncertainty associated with a quantity Y that is a function of Q other quantities x_i such as $Y = f(x_1, x_2, ..., x_Q)$ requires to propagate the uncertainties of the inputs x_i through the functional relationship f. The absolute uncertainty associated with the estimate y of the measurand Y that depends on the uncorrelated parameters x_i is given by the *law of propagation of uncertainty* (cf. [1], Sec. 5.1.2, Eq. 10, or [2], Eq. 2):

$$\sigma_y^2 = \sum_{i=1}^{Q} \left(\frac{\partial f}{\partial x_i} \right)^2 \sigma_{x_i}^2 \tag{S7}$$

This law is obtained by a first order Taylor expansion and is valid as long as the nonlinearity of f remains insignificant. Otherwise, the terms of higher order should also be taken into account.

In case the parameters x_i are correlated, it is necessary to take into account the contribution of correlation coefficients defined as $r(x_i, x_j) = \frac{cov(x_i, x_j)}{\sigma_{x_i} \sigma_{x_j}}$. The law of propagation then becomes:

$$\sigma_y^2 = \sum_{i=1}^{Q} \left(\frac{\partial f}{\partial x_i} \right)^2 \sigma_{x_i}^2 + 2 \sum_{i=1}^{Q-1} \sum_{j=i+1}^{Q} \frac{\partial f}{\partial x_i} \frac{\partial f}{\partial x_j} \sigma_{x_i} \sigma_{x_j} r(x_i, x_j) \tag{S8}$$

B. Incident flux

The calibration of the incident flux Φ_{i,Δ_λ} per spectral interval of interest defined as a central wavelength λ_0 and an associated bandwidth Δ_λ is performed using the equation:

$$\Phi_{i,\Delta_\lambda} = \pi D_s^2 \frac{(1 - \rho(1 - \alpha))}{\rho} E_{\Delta_\lambda} \tag{S9}$$

where $\alpha = \frac{A_i + A_o}{\pi D_s^2}$ is the fraction of the sphere that is occupied by the opened ports.

The incident flux depends on the integrating sphere parameters (sphere diameter D_s, area of the entrance and exit port A_i and A_o, coating albedo ρ) and on the spectral irradiance $E_{\Delta\lambda}$ measured at the exit port of the sphere. Only power functions are involved in Eq. S9, so its uncertainty is estimated applying Eq. S7:

$$\begin{aligned} \sigma^2(\Phi_{i,\Delta_\lambda}) = &\left(\frac{\partial \Phi_{i,\Delta_\lambda}}{\partial D_s} \right)^2 \sigma_{D_s}^2 + \left(\frac{\partial \Phi_{i,\Delta_\lambda}}{\partial A_i} \right)^2 \sigma_{A_i}^2 + \left(\frac{\partial \Phi_{i,\Delta_\lambda}}{\partial A_o} \right)^2 \sigma_{A_o}^2 + \left(\frac{\partial \Phi_{i,\Delta_\lambda}}{\partial \rho} \right)^2 \sigma_\rho^2 \\ &+ \left(\frac{\partial \Phi_{i,\Delta_\lambda}}{\partial E_{\Delta\lambda}} \right)^2 \sigma^2(E_{\Delta\lambda}) \end{aligned} \tag{S10}$$

The partial derivatives are quite straightforward to compute from Eq. S9, as detailed in Eq. S11.

$$\begin{cases} \frac{\partial \Phi_{i,\Delta_\lambda}}{\partial D_s} = \frac{2\pi(1-\rho) D_s E_{\Delta\lambda}}{\rho} \\ \frac{\partial \Phi_{i,\Delta_\lambda}}{\partial A_i} = \frac{\partial \Phi_{i,\Delta_\lambda}}{\partial A_o} = E_{\Delta\lambda} \\ \frac{\partial \Phi_{i,\Delta_\lambda}}{\partial \rho} = -\frac{\pi D_s^2 E_{\Delta\lambda}}{\rho^2} \\ \frac{\partial \Phi_{i,\Delta_\lambda}}{\partial E_{\Delta\lambda}} = \pi D_s^2 \frac{1 - \rho(1 - \frac{A_i + A_o}{\pi D_s^2})}{\rho} \end{cases} \tag{S11}$$

It is however necessary to estimate the uncertainties related to each of the involved parameters.

Albedo: The sphere coating albedo is given by the manufacturer, for multiple wavelengths. It is constant over the visible spectral range and has a value of $\rho = 0.99 \pm \sigma_\rho$. According to the calibration certificate of Labsphere white diffuser with such range of albedo [3], the associated uncertainty is $\sigma_\rho = 0.00265$ for every wavelength of interest.

Sphere diameter: The sphere diameter is given by the manufacturer, without specifying an associated uncertainty. Therefore we took the accuracy of the given value as the uncertainty: $D_s = 13.462 \pm 0.001$ cm.

Area of entrance and exit ports: According to the manufacturer specifications, the diameters of the circular ports of the sphere are $D = 2.54 \pm 0.01$ cm. Since these parameters are easy to measure, we reduced such uncertainty by proceeding to the measurement of these each diameter using a caliper with graduations 0.01 cm. By performing ten measurements of each port, we were able to statistically compute using Equation S4 a diameter for the entrance port of $D_i = 2.509 \pm 0.004$ cm and a diameter for the exit port of $D_o = 2.526 \pm 0.003$ cm.

The uncertainties associated with the areas $A = \pi(D/2)^2$ are computed by applying the rule from Eq. S7 where the corresponding diameter D is the only variable that comes with an uncertainty σ_D:

$$\sigma_A^2 = \left(\frac{\partial A}{\partial D}\right)^2 \sigma_D^2 = \left(\frac{\pi D}{2}\right)^2 \sigma_D^2 \tag{S12}$$

obtaining respectively $A_i = 4.944 \pm 0.015$ cm^2 and $A_o = 5.011 \pm 0.011$ cm^2.

Irradiance per spectral interval: The sekonic Spectromaster C-7000 spectrometer we used to measure the spectral irradiance at the exit port of the integrating sphere has an accuracy of $\pm 5\% \pm 1$ digit with 1 $digit = 10^{-12}$ given by the manufacturer. Therefore, using Equation S6, the absolute uncertainty on a single spectral irradiance measurement induced by such device is defined by:

$$\sigma_{E_m(\lambda)} = \frac{0.05 E_m(\lambda) + 10^{-12}}{\sqrt{3}} \tag{S13}$$

For a more accurate estimation of the spectral irradiance, we proceed to 5 measurements $E_m(\lambda)$ under the same conditions and to the averaging of the acquired spectra defining the mean irradiance $E(\lambda)$. The related uncertainty is then computed using the statistical approach from Equation S4:

$$\sigma_{E(\lambda)}^2 = \frac{1}{5 \times 4} \sum_{m=1}^{5} (E_m(\lambda) - E(\lambda))^2 \tag{S14}$$

Finally, the irradiance per spectral interval of interest $E_{\Delta\lambda}$ is defined as the spectral irradiance integrated over the measurement spectral range ($[\lambda_\mu = 380,\ \lambda_M = 780]$ nm with a step of 1 nm). Using the trapezoidal integration rule, we obtain:

$$E_{\Delta\lambda} = \int_{\lambda_\mu}^{\lambda_M} E(\lambda) \mathrm{d}\lambda = \sum_{w=\mu}^{M-1} \frac{\lambda_{w+1} - \lambda_w}{2} (E(\lambda_w) + E(\lambda_{w+1})) \tag{S15}$$

Applying Eq. S7 to propagate the spectral irradiance uncertainties through the integration process of Eq. S15 leads to the actual uncertainty of the total irradiance at a given spectral interval:

$$\sigma_{E_{\Delta\lambda}}^2 = \sum_{w=\mu}^{M-1} \left(\frac{\lambda_{w+1} - \lambda_w}{2}\right)^2 [\sigma_{E(\lambda_w)}^2 + \sigma_{E(\lambda_{w+1})}^2] \tag{S16}$$

This uncertainty depends on the spectral interval of interest. It is computed for each of the 13 intervals we used during BSSxDF acquisition.

Results and discussion: The total incident flux uncertainty is then computed by combining Eq. S10 with the absolute uncertainties estimated for each of the parameters. As a result, we obtained a relative uncertainty of about 9.8% for each of the studied spectral interval.

By analysing the value of each term of the sum in Eq. S10, it is noticeable that the one with respect to the albedo ρ has the more influence. Indeed, a small variation of the uncertainty associated with ρ involves an important variation of the incident flux relative uncertainty (cf. Fig. S1a). It is this term that must be improved as a priority in order to reduce the total flux uncertainty. If its uncertainty were smaller the flux relative uncertainty would decrease and the influence of other parameters involved in the flux would more significant (cf. Fig. S1b). However the uncertainty associated with this parameter comes from very accurate calibration processes developed in metrological facilities, so it is already the smallest currently available value. This analysis demonstrates that we have reached the best evaluation of the absolute flux that we could make using our calibration protocol.

Another solution to reduce the uncertainty on the flux would be to opt for another calibration method.

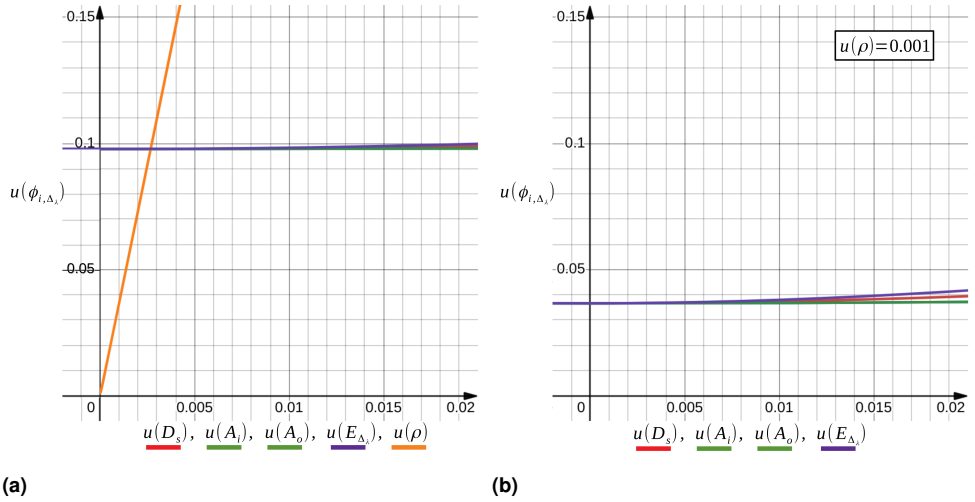

Fig. S1. Dependence of the incident flux relative uncertainty $u(\Phi_{i,\Delta_\lambda}) = \frac{\sigma(\Phi_{i,\Delta_\lambda})}{\Phi_{i,\Delta_\lambda}}$ on the relative uncertainties of the parameters D_s, A_i, A_o, E_{Δ_λ}, and ρ. The influence of the parameters uncertainties are analyzed separately. The curves are obtained with Equations S10 and S9 while fixing all the parameters relative uncertainties except the one whose influence is studied. (a) When fixed, the relative uncertainties of the parameters have the value determined in our calibration process. The uncertainty of the integrating sphere albedo ρ has the more influence: a small variation of this parameter involves an important change in the flux relative uncertainty. When it is fixed ($u(\rho) = 0.00267$ according to the manufacturer) the influence of the other parameters uncertainties are negligible. (b) When fixed at a smaller value ($u(\rho) = 0.001$), the uncertainty on the flux is much smaller, and the influence of the other parameters uncertainties becomes more visible.

C. Observed radiance

The conversion from pixel value to radiance is performed using the equation:

$$L_{s,\Delta_\lambda}(i,j) = \frac{4(m+1)^2 f_\sharp^2}{A_p \pi g(i,j)} \frac{f^{-1}(V_{\Delta\lambda}(i,j))}{t_e} \tag{S17}$$

It depends on the camera acquisition parameters (aperture $f_\sharp$ and exposure time t_e), on the distance between the camera and the object (magnification m), on the sensor characteristics (pixel area A_p and spatial non-uniformity corrected by the flat field $g(i,j)$), and on the camera response f^{-1} . Only power functions are involved in Eq. S17, so its uncertainty is estimated applying Eq. S7:

$$\begin{aligned}\sigma^2(L_{s,\Delta_\lambda}(i,j)) = &\left(\frac{\partial L_{s,\Delta_\lambda}}{\partial f_\sharp}\right)^2 \sigma^2_{f_\sharp} + \left(\frac{\partial L_{s,\Delta_\lambda}}{\partial t_e}\right)^2 \sigma^2_{t_e} + \left(\frac{\partial L_{s,\Delta_\lambda}}{\partial m}\right)^2 \sigma^2_m \\ &+ \left(\frac{\partial L_{s,\Delta_\lambda}}{\partial A_p}\right)^2 \sigma^2_{A_p} + \left(\frac{\partial L_{s,\Delta_\lambda}}{\partial g(i,j)}\right)^2 \sigma^2_{g(i,j)} + \left(\frac{\partial L_{s,\Delta_\lambda}}{\partial f^{-1}}\right)^2 \sigma^2_{f^{-1}}\end{aligned} \tag{S18}$$

Aperture and exposure time: The aperture and the exposure time are discrete variables of the camera that are given by the manufacturer. In our experiment, we used fixed values, and we considered both uncertainties related to these parameters as negligible.

Pixel area: The size of a square pixel of the sensor is given by the manufacturer as $s_p = 5.35 \pm 0.005$ µm. The pixel area is computed as the square of the pixel size: $A_p = 28.6 \pm 0.0535\ \mu m^2$.

Magnification: Theoretically the magnification is defined on the optical axis. So as a first approximation we consider only one value of the magnification for every pixel of the sensor.

It can be computed as the ratio between the image size over the object size. Imaging a ChArUco board, we have a well defined object with size known up to a negligible uncertainty. We used

the same board as the one from camera calibration, with the ArUco markers of size s_A such as $s_A \times s_A = 9 \times 9$ mm^2 (cf. Fig. S2a).

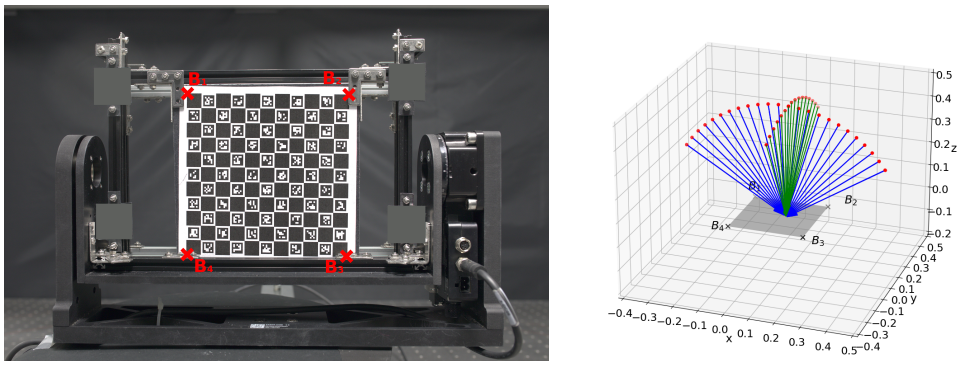

(a) (b)

Fig. S2. (a) Image of the ChArUco board used for the camera calibration, at normal observation. The checkerboard has a square size of 12×12 mm^2, and the ArUco markers have a square size of 9×9 mm^2. (b) Positions of the camera (red dots) that are used for the geometric calibration, relatively to the sample's front face defined by the points $\mathbf{B_{1..4}}$. Blue arrows correspond to the camera directions that are in the incident plane ($\phi_p = 0°$ or $180°$), while green arrows correspond to camera directions in the transversal plane ($\phi_o = 90°$ or $270°$).

By noting c the length in pixels of the side of an ArUco marker on the image of the ChArUco board taken at normal observation (camera facing the board), and s_p the pixel size, the magnification of the $k-$th marker is defined as:

$$m_k = \frac{s_p c}{s_A} \tag{S19}$$

with an associated uncertainty:

$$\sigma_{m_k}^2 = \left(\frac{\partial m_k}{\partial s_p}\right)^2 \sigma_{s_p}^2 + \left(\frac{\partial m_k}{\partial c}\right)^2 \sigma_c^2 \tag{S20}$$

The uncertainty on the pixel size has already been studied in previous section. Then in order to compute the magnification uncertainty, one must compute the uncertainty associated with c.

Let's denote A, B, C and D the four corners of one detected ArUco marker. The size of the corner's side is defined as the euclidian distance in pixels between to adjacent corners. Therefore four values of c can be computed per marker, one for each size of the square shape. As an example, the lengths c_{AB} between corners $A(i_A, j_A)$ and $B(i_B, j_B)$ is written:

$$c_{AB} = AB = \sqrt{(i_B - i_A)^2 + (j_B - j_A)^2} \tag{S21}$$

During the camera model calibration process, the re-projection error was estimated to $\sigma_P = 0.61$ pixels $= 44.7$ µm. Then both coordinates i and j of a corner are detected with an error of $\pm\sigma_P$. The propagation of this uncertainty to c_{AB} is obtained by applying Eq. S7 to Eq. S21:

$$\sigma_{c_{AB}}^2 = 2\left(\frac{i_B - i_A}{c}\right)^2 \sigma_P^2 + 2\left(\frac{j_B - j_A}{c}\right)^2 \sigma_P^2 \tag{S22}$$

The results over the four segments of the studied ArUco marker are averaged to obtain the mean c value. Here, because we are not averaging over four measurements of the same segment but on the measurement of four different segment of supposed same dimensions, it is not possible to establish a statistical error from Equation S3. It is necessary to apply the propagation rule from Equation S7:

$$\sigma_c^2 = \frac{1}{4^2} \sum_{XY \in [AB,BC,CD,DA]} \sigma_{c_{XY}}^2 \tag{S23}$$

For the image at normal incidence that we are considering, a total of N Aruco markers are actually detected. So the magnification is defined as the averaged over the magnification values computed for each detected marker:

$$m = \frac{1}{N} \sum_{k=1}^{N} m_k \tag{S24}$$

Again the uncertainty propagates according to Equation S7. The total uncertainty associated with the magnification is:

$$\sigma_m = \sqrt{\frac{1}{N^2} \sum_{k=1}^{N} \sigma_{m_k}^2} = 1.8 \times 10^{-5} \tag{S25}$$

Flat field: Since the flat field accounts for the non uniformity over the camera sensor, it is pixel dependent. Therefore its associated uncertainty is a 2D map of same size as the sensor (in pixels) (see Figure S4).

Although we proceed to the averaging over $N = 10$ acquisitions to measure the flat field in order to reduce the variance of the measurement, the results remain quite noisy as shown on Figure S3. That is why we modeled the flat field, using two different models: the cosine fourth law that is commonly used in the literature [4], and a third polynomial. The parameters of the fitted models are optimized using mean squares. Assuming that the flat field presents a symmetry around the optical axis, the modeling is performed on the longitudinal profile of the measurement. Results obtained for each RGB channel are illustrated on Figure S3. The third polynomial allows a better fit to the measurements, correctly modeling the vignetting on the sides of the pictures, while the intensity fall off modeled by the cosine fourth law is too steep. In the following and in the main paper we used the third degree polynomial as a flat field model.

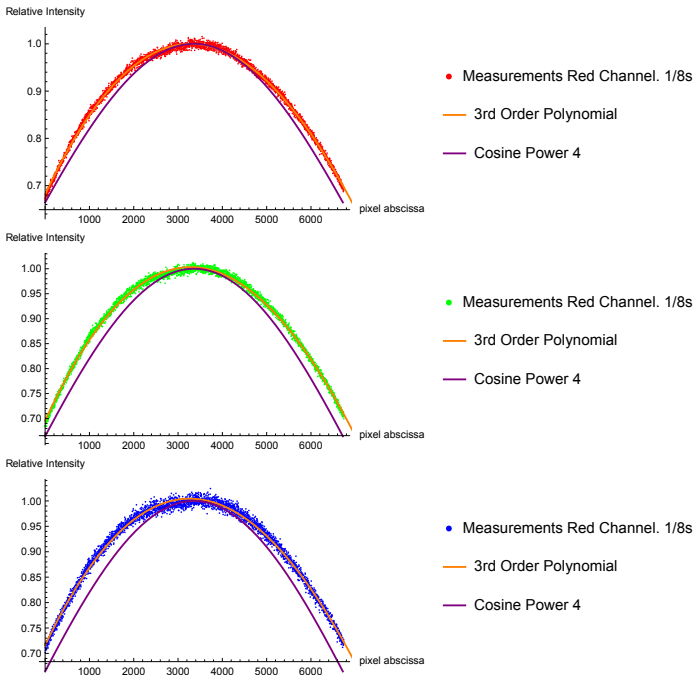

Fig. S3. Flat field profiles of the three channels of the camera sensor. The measurements are quite noisy, therefore the flat field is modeled using the cosine fourth law and a third degree polynomial. The third polynomial allows a better fitting of the measurements, correctly modeling the vignetting on the sides of the pictures, while the intensity fall off modeled by the cosine fourth law is too steep.

On each pixel of the sensor, the modeling uncertainty is computed as the root mean square error between the flat field measurements and the prediction using the fitted polynomial at this pixel.

$$\sigma_{g(i,j)} = \sqrt{\frac{\sum_{i=1}^{N}(y_i - y)^2}{N}} \tag{S26}$$

where y_i are the measurements on one pixel, y is the prediction at this pixel, and N is the number of measurements.

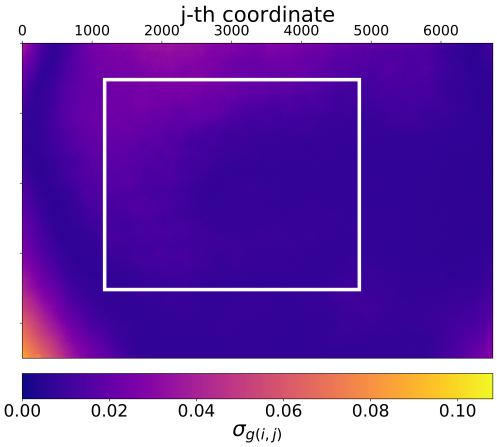

Fig. S4. Flat field uncertainty map. The highest error are reached on the very sensor's sides. For a smaller region of interest in the pictures (delimited by the white rectangle) that is effectively imaging the sample, $\sigma_{g(i,j)} \leqslant 0.1$.

The maximum uncertainty values lie on the sides where the vignetting effect introduced by the camera lens has more influence. At the center of an image, the uncertainty would not exceed $\sigma_{g(i,j)} = 0.1$.

To remove the flat field symmetry of revolution assumption requires to use a 2D model. Figure S5 shows the results obtained for the fitting of the red channel flat field using a bivariate quadratic polynomial model. The fitting results in the model expressed in Equation S27.

$$g(x,y) = -0.086918x^2 + 0.00286643xy + 0.0275485x - 0.0548976y^2 + 0.0137671y + 0.996458 \tag{S27}$$

Contrary to the modeling on the one dimensional profiles (cf. Fig. S3), the asymmetry properties of the measured flat field are taken into account during the fitting process, therefore smaller errors are obtained. The maximum obtained error is $\sigma_{g(i,j)} = 0.038$.

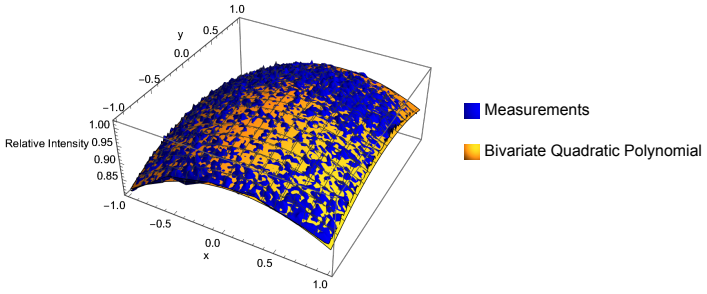

Fig. S5. Modeling of the red channel flat field using a bivariate polynomial. The mean square error is 4×10^{-5}, leading to a maximum error between the measurement and the fitting of 0.038.

Camera inverse response: After the camera calibration measurements, it appears that the RGB response linearity depends on the spectral interval of interest. For a interval where none of the channel reaches the saturation level, all channels show a nearly linear response. However, for other intervals where at least one channel reaches the saturation level there is a distinction between the saturated channels that show a linear response, and the non saturated channels that don't (see Figure S6).

For each spectral interval of interest, the inverse response of the RGB channels is fitted on the non saturated measurements using either a linear model, or a third degree polynomial, according to Eq. S28. The choice of a third degree polynomial allows both a good fitting of the measurement data and relatively small uncertainties of the fitted parameters (cf. Figure S6). Smaller polynomial degree would deteriorate the quality of the fit while larger degree would increase the fitted parameters uncertainties because of an overfitting of the data. By definition, the camera response and so the inverse response is null when no light is incoming on the sensor, and strictly positive otherwise. The fits are then performed under the constrained $f^{-1}(0) = 0$, minimizing the squared error between the model and the measurements.

$$f^{-1}(x) = \begin{cases} ax, & \text{if channel reaches saturation.} \\ ax^3 + bx^2 + cx, & \text{otherwise.} \end{cases} \tag{S28}$$

The variance of the estimated a, b and c parameters of the models is given by the diagonal of covariance matrix of the fit. The total uncertainty of the fit $\sigma_{f^{-1}}$ is then computed by propagating the uncertainties σ_a, σ_b and σ_c along the model using Eq. S7.

$$C = \begin{bmatrix} \sigma_a^2 & \sigma_a\sigma_b & \sigma_a\sigma_c \\ \sigma_b\sigma_a & \sigma_b^2 & \sigma_b\sigma_c \\ \sigma_c\sigma_a & \sigma_c\sigma_b & \sigma_c^2 \end{bmatrix} \tag{S29}$$

With this modeling, we can estimate the uncertainty that is related to the inverse camera response. This is done by applying Eq. S7 on the inverse response model of Eq. S28:

$$\sigma_{f^{-1}}^2 = \left(\frac{\partial x}{\partial a}\sigma_a\right)^2 + \left(\frac{\partial x}{\partial b}\sigma_b\right)^2 + \left(\frac{\partial x}{\partial c}\sigma_c\right)^2 \tag{S30}$$

It results that the relative uncertainty on the camera inverse response does not exceed 1% whatever spectral interval is at stake (cf. Fig. S7).

Results and discussion: The total uncertainty associated with the observed radiance is sample dependent and is computed by evaluating Eq. S18. We obtained a maximum relative uncertainty of 13.6% for both samples.

Among the different terms in Eq. S18, the term relative to the uncertainty on the inverse camera response appears to be the main source of error. In order to improve the accuracy on this term, it would be of great interest to use a scientific camera with available data of the camera response. Since these data would be calibrated in metrological facilities, we expect them to be more reliable than the one we obtained through our simple calibration protocol.

D. Geometric Uncertainties

The spatio-angular parameters involved in the BSSxDF definition are retrieved using ray-tracing from the camera to the first intersection with a virtual mesh with same dimensions as the studied sample. The associated uncertainties depend on the sources of errors encountered during the geometric calibration procedure.

Triangulation: The position of the sample with respect to the camera is defined by the position of the four vertices $\mathbf{B}_{1..4}$ of its front plane that are computed through a triangulation process. Thanks to the camera calibration procedure, projection matrices that convert a position in world space to pixels coordinates in image space are known for a set of rotation stages configurations. A subset of $N = 9$ rotation stages positions among these known configurations are used to image the sample of interest in ambient light. The triangulation process is performed using Direct Linear Transform (DLT) [5] on only half of the subset. The other configurations are used to assess the robustness of our procedure and establish the related uncertainties.

Points $\mathbf{B}_{1..4}$ are first manually selected across the N pictures. The selected pixels coordinates from $N - 4$ configurations are triangulated to obtain the corresponding positions in world space.

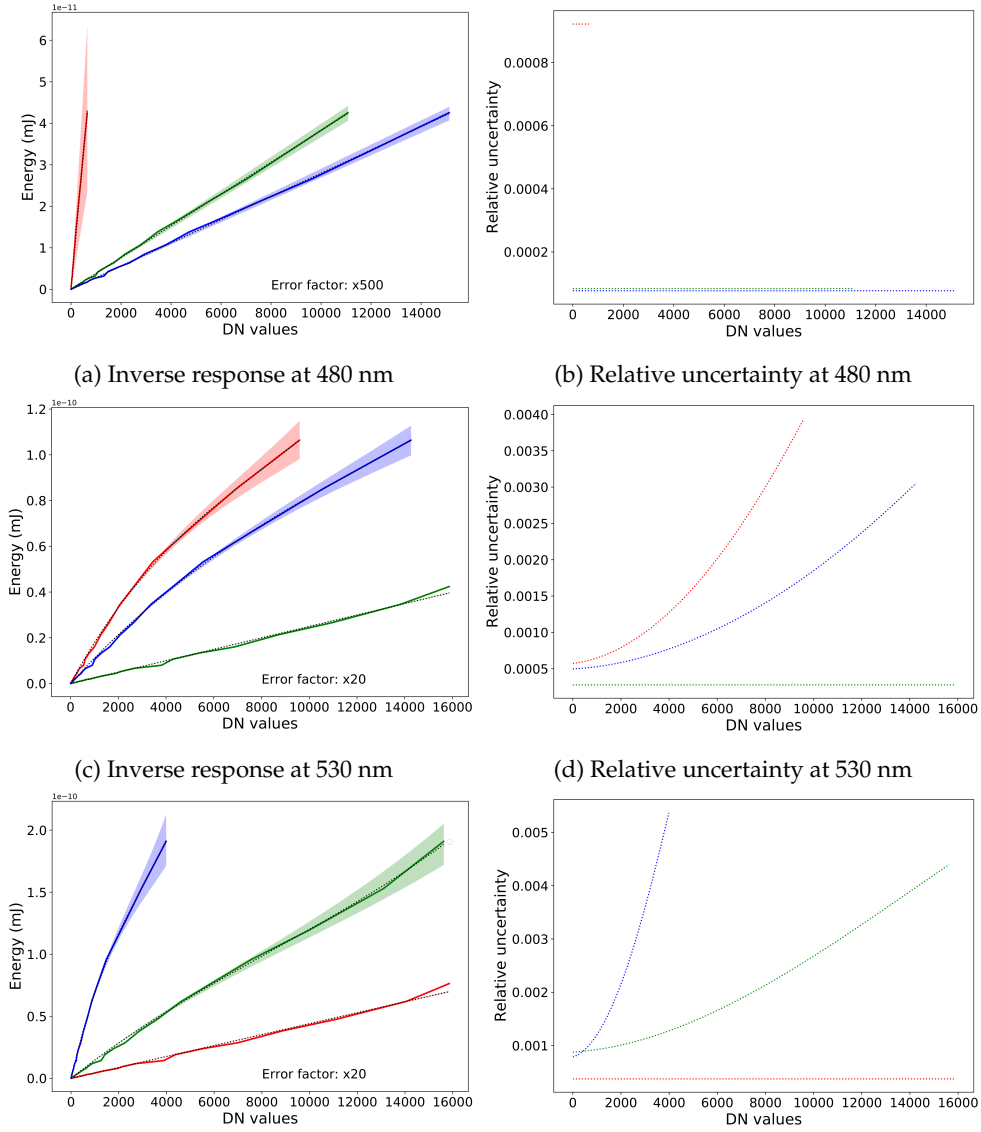

(a) Inverse response at 480 nm

(b) Relative uncertainty at 480 nm

(c) Inverse response at 530 nm

(d) Relative uncertainty at 530 nm

(e) Inverse response at 610 nm

(f) Relative uncertainty at 610 nm

Fig. S6. RGB channels inverse response. (a, c, e) The measurements at a specific spectral interval are fitted using analytical models. The larger color dots correspond to the inverted measurements, the dotted lines represent the modeling using the analytical models (cf. Eq. S28). The errors (colored areas) are scaled for visibility. (b, d, f) Relative uncertainty associated with the fits. The more sensitive channels that are fitted using a linear model show a very small uncertainty. For other channels, the uncertainty is increasing with the DN value.

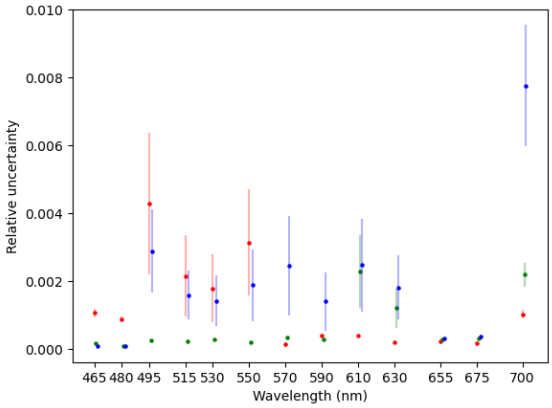

Fig. S7. Camera inverse response relative uncertainty per spectral interval. For all the intervals of interest, the mean relative uncertainty does not exceed 1% of the inverse response value. The more a channel is sensitive to the incoming wavelength, the lower is the uncertainty and its variance.

The resulting 3D points are re-projected on the pictures of the 4 unused configurations. The uncertainty associated with the vertices positions $\sigma_{\mathbf{B}_{1..4}}$ is then defined as the maximum distance between the projected pixels coordinates and the previously selected ones, resulting in a value of about 22.5 pixels. Using the pixels size $s_p = 5.35$ µm and the magnification $m = 0.073$, this corresponds to an uncertainty $\sigma_{\mathbf{B}_{1..4}} = 1.6$ mm.

Motor axes: The uncertainties of the spatio-angular parameters retrieved through ray-tracing for a given configuration of the rotation stages depend on the accuracy of the camera position transformation estimated using the axes and centers of rotation determined with the motor axes calibration (cf. Section 4.2.3. of the main paper). Each position of the camera being reached by a given combination of the motor angles m_0, m_1, and m_2, the rotation of the camera relative to its original position (along the sample's surface normal, pointing towards the sample) is defined by the matrix R_c such as:

$$R_c = R_{\mathbf{x'_2}}(m_2)R_{\mathbf{y'_1}}(m_1)R_{\mathbf{y'_0}}(m_0) \tag{S31}$$

where R_X is the rotation matrix around the axis X, and $\mathbf{x'_k}$ and $\mathbf{y'_k}$ are the calibrated rotation axes of the rotation stage M_k mainly rotating around the x-axis or y-axis respectively.

The rotation axis of a rotation stage is computed as the normal to the plane that fits the movement of a specific point of the sample surface across pictures taken for different motor angles. Imaging a ChArUco board in different angular configuration (cf. Fig S2) allows to analyze the movement of N_A ArUco markers. The rotation axis is then averaged over the normals of N_A fitted planes, leading to the following results:

$$\begin{cases} \mathbf{y'_0}(2.139 \times 10^{-2},\ 0.9995,\ -2.213 \times 10^{-2}) \\ \mathbf{y'_1}(2.008 \times 10^{-2},\ 0.9995,\ -2.227 \times 10^{-2}) \\ \mathbf{x'_2}(0.9999,\ -2.197 \times 10^{-3},\ -1.347 \times 10^{-2}) \end{cases} \tag{S32}$$

When the plane fits are considered as perfect, the associated uncertainties are defined as the standard deviation to the normal values, giving:

$$\begin{cases} \sigma_{\mathbf{y'_0}} = (\pm 4.3 \times 10^{-3},\ \pm 8.1 \times 10^{-5},\ \pm 1.4 \times 10^{-3}) \\ \sigma_{\mathbf{y'_1}} = (\pm 5.7 \times 10^{-3},\ \pm 1.3 \times 10^{-4},\ \pm 8.4 \times 10^{-3}) \\ \sigma_{\mathbf{x'_2}} = (\pm 3.5 \times 10^{-5},\ \pm 7.7 \times 10^{-3},\ \pm 1.9 \times 10^{-3}) \end{cases} \tag{S33}$$

A more complete uncertainty analysis would require to take into account the quality of the fit. The planes with normal $\mathbf{n}(n_x, n_y, n_z)$ were determined using singular value decomposition (SVD). The squared uncertainties associated with the normal coordinates $(\sigma^2_{n_x}, \sigma^2_{n_y}, \sigma^2_{n_z})$ can be established as the diagonal of the fit covariance matrix. The uncertainties then propagates through

the averaging process over the N_A normals (cf. Eq. S34) leading to the actual uncertainty related to the calibrated axes.

$$(\sigma_{n_{x'}}, \sigma_{n_{y'}}, \sigma_{n_{z'}}) = \sqrt{\frac{1}{N_A^2} \sum_{k=1}^{N_C} (\sigma_{n_x}^2, \sigma_{n_y}^2, \sigma_{n_z}^2)} \tag{S34}$$

In this case, we obtained the following results:

$$\begin{cases} \sigma_{\mathbf{y'_0}} = (\pm 5.3 \times 10^{-2},\ \pm 1.2 \times 10^{-3},\ \pm 1.5 \times 10^{-2}) \\ \sigma_{\mathbf{y'_1}} = (\pm 7.5 \times 10^{-2},\ \pm 1.7 \times 10^{-3},\ \pm 2.1 \times 10^{-2}) \\ \sigma_{\mathbf{x'_2}} = (\pm 5.9 \times 10^{-4},\ \pm 5.1 \times 10^{-2},\ \pm 1.2 \times 10^{-2}) \end{cases} \tag{S35}$$

Considering the plane fitting as another source of error tends to increase the rotation axes uncertainties. For the coordinates that have a very small influence on the axis direction (eg. coordinates y'_{0x} and y'_{0z} for axis $\mathbf{y'_0}$), their nominal values are so small that the associated relative uncertainties (eg. $\sigma_{y'_{0x}}/y'_{0x}$ and $\sigma_{y'_{0z}}/y'_{0z}$ for axis $\mathbf{y'_0}$) cannot be well defined. However, the uncertainties relative to the main coordinate of each rotation stage axis (eg. coordinates y'_{0y} for axis y'_0) remain very small (about 0.1%).

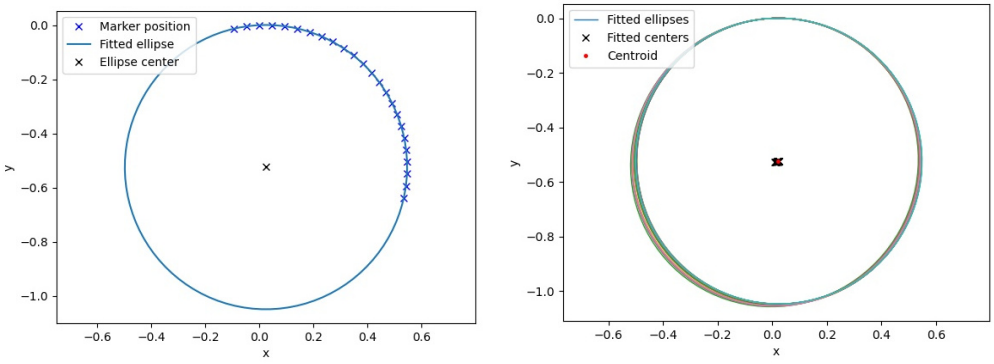

(a) Fitting of the movement of one ArUco marker. **(b)** Averaging over multiple ArUco markers.

Fig. S8. Determination of the rotation center of the motorized rotation stage M_0. (a) When rotating the rotation stage, the position of each ArUco marker defines an ellipse around the rotation axis. The rotation center is defined as the center of the fitted ellipse. (b) The results obtained for every markers are averaged to define the calibrated rotation center c.

To compute the rotation center, the 3D positions of a given ArUco marker are projected onto the fitted plane and their 2D coordinates are fitted with an ellipse [6] (cf Figure S8a). The center of the ellipse is then re-projected into world space. The rotation center $c_k = (c_{xk}, c_{yk}, c_{zk})$ of each rotation stage k is averaged over the centers of the ellipses obtained for the N_A considered markers (cf Figure S8b). In the ideal case of a perfect fit, its uncertainty $\sigma_{c_k} = (\sigma_{c_{xk}}, \sigma_{c_{yk}}, \sigma_{c_{zk}})$ is defined as the standard deviation. The centroid of the 3D positions, in meters, of all three rotation stages defines the nominal coordinates of the calibrated center c of the whole system (cf. Eq. S36):

$$c = \begin{cases} (4.9 \times 10^{-2},\ 2.1 \times 10^{-2},\ 3.3 \times 10^{-3})\text{m}, & \text{if elliptical fit.} \\ (4.8 \times 10^{-2},\ 2.0 \times 10^{-2},\ 4.0 \times 10^{-3})\text{m}, & \text{if circular fit.} \end{cases} \tag{S36}$$

The uncertainties σ_{c_k} then propagates towards the calibrated center uncertainty σ_c (cf. Eq. S37):

$$\sigma_c = \begin{cases} (\pm 4.2 \times 10^{-4},\ \pm 3.7 \times 10^{-3},\ \pm 1.0 \times 10^{-2})\text{m}, & \text{if elliptical fit.} \\ (\pm 2.0 \times 10^{-4},\ \pm 1.0 \times 10^{-4},\ \pm 2.3 \times 10^{-3})\text{m}, & \text{if circular fit.} \end{cases} \tag{S37}$$

Again, the complete uncertainty analysis should account for the actual uncertainties associated with the ellipse fitting. The uncertainties on the fitted parameters of the ellipse conic section formula are computed according to [7]. These are propagated through the conversion into 2D ellipse center, the re-projection into world space, and through the averaging procedures to obtain the uncertainty of the calibrated rotation center (cf. Eq. S38).

$$\sigma_c = \begin{cases} (\pm 0.15,\ \pm 0.21,\ \pm 0.47)\text{m}, & \text{if elliptical fit.} \\ (\pm 0.047,\ \pm 0.049,\ \pm 0.096)\text{m}, & \text{if circular fit.} \end{cases} \tag{S38}$$

The uncertainties obtained while accounting for the ellipse fitting are much larger than the one only accounting for the averaging over the multiple considered ArUco markers. This may be due to two reasons. First, using an elliptical model amounts to optimizing 6 parameters, which may lead to an over-fitting of the available data. Apart from the ellipse center position, its dimension, its orientation and its eccentricity are also optimized. Regarding the small eccentricity values, it appears that using a circular model would be sufficient while reducing the number of optimization parameters (center 2D position and radius) and therefore their associated uncertainties. Applying such model indeed improves the uncertainties of one order of magnitude (cf. Eq S38), but these remain quite high relatively to the mean rotation center c (cf. Eq. S36). Another factor that limits the fit accuracy is the number of 2D coordinates used as inputs. Since the ChArUco board is opaque, and because of the sample holder masking, markers can only be detected in the reflection hemisphere for a limited range of rotation stages configurations. This leads to a lacunar set of 2D marker positions on which the fit is based (cf. Fig. S8a).

Assuming a π symmetry of the markers positions in the rotation plane around the rotation center determined through an elliptical (or circular) fitting allows to double the number of studied markers. Performing a new fit with these additional inputs gives similar rotation center (cf. S39) nominal values with smaller uncertainties (cf. S40).

$$c = \begin{cases} (4.8 \times 10^{-2},\ 2.1 \times 10^{-2},\ 3.2 \times 10^{-3})\ \text{m}, & \text{if elliptical fit.} \\ (4.8 \times 10^{-2},\ 2.0 \times 10^{-2},\ 4.1 \times 10^{-3})\ \text{m}, & \text{if circular fit.} \end{cases} \tag{S39}$$

$$\sigma_c = \begin{cases} (\pm 0.043,\ \pm 0.044,\ \pm 0.044)\ \text{m}, & \text{if elliptical fit.} \\ (\pm 0.036,\ \pm 0.035,\ \pm 0.034)\ \text{m}, & \text{if circular fit.} \end{cases} \tag{S40}$$

A more accurate way to increase the number of studied markers would be to use a two-sided ChArUco board so that markers can be detected in the transmission hemisphere too.

Spatial uncertainties: The BSSxDF spatio-angular parameters are retrieved through ray tracing from the camera to a mesh of same size as the sample (cf. Sec. 5.2. of the main paper). The spatial parameters that are the position of the illumination spot $\mathbf{x_i}$ and the position of the observation point $\mathbf{x_r}$ on the sample are then directly related to the accuracy of the mesh rigid transformation (cf. first paragraph of Sec. D): Every coordinates of the positions $\mathbf{x_i}$ and $\mathbf{x_r}$ has an absolute uncertainty of 1.6 mm:

$$\sigma_{x_i} = \sigma_{x_r} = \sigma_{y_i} = \sigma_{y_r} = \sigma_{z_i} = \sigma_{z_r} = \sigma_{\mathbf{B}_{1..4}} \tag{S41}$$

It is noticeable that these uncertainties are completely correlated, since x_i and x_r are both affected in the same way by the rigid transformation of the mesh. As a consequence, a variation of $\pm\delta_x$ on the coordinate x_i (resp. $+\delta_y$ on the coordinate y_i and $+\delta_z$ on the coordinate z_i) implies a variation of $\pm\delta_x$ on the coordinate x_r (resp. $+\delta_y$ on the coordinate y_r and $+\delta_z$ on the coordinate z_r). The correlation coefficient between the coordinates $c \in \{x, y, z\}$ can be expressed as:

$$r(c_i, c_r) = \frac{cov(c_i, c_i)}{\sigma_{c_i}\sigma_{c_r}} = \frac{cov(c_r, c_r)}{\sigma_{c_i}\sigma_{c_r}} = 1 \tag{S42}$$

Another spatial parameter is the distance between the illumination spot and the observation point defined as $d_r = |\mathbf{x_i} - \mathbf{x_r}|$ for $\mathbf{x_r}$ located on the sample front face, and $d_t = |\mathbf{x_{i,\perp}} - \mathbf{x_t}|$ for $\mathbf{x_t}$ located on the back face of the sample and $x_{i,\perp}$ the orthogonal projection of $\mathbf{x_i}$ onto the back face. By applying the propagation rule from Equation S8, and using Equation S41, it follows that the uncertainty on this new parameter is:

$$\begin{aligned} \sigma_d^2 &= \left(\frac{\partial d}{\partial x_i}\sigma_{x_i}\right)^2 + \left(\frac{\partial d}{\partial x_r}\sigma_{x_r}\right)^2 + \left(\frac{\partial d}{\partial y_i}\sigma_{y_i}\right)^2 + \left(\frac{\partial d}{\partial y_r}\sigma_{y_r}\right)^2 + \left(\frac{\partial d}{\partial z_i}\sigma_{z_i}\right)^2 + \left(\frac{\partial d}{\partial z_r}\sigma_{z_r}\right)^2 + C \\ &= 2\left(\frac{\partial d}{\partial x_i}\sigma_{x_i}\right)^2 + 2\left(\frac{\partial d}{\partial y_i}\sigma_{y_i}\right)^2 + 2\left(\frac{\partial d}{\partial z_i}\sigma_{z_i}\right)^2 + C \end{aligned} \tag{S43}$$

where C groups the correlation terms between x_i and x_r, y_i and y_r, z_i and z_r. Using Equation S42 and the equality $\frac{\partial d}{\partial c_i} = -\frac{\partial d}{\partial c_r}$ with $c \in \{x, y, z\}$:

$$\begin{aligned} C &= 2r(x_i, x_r)\frac{\partial d}{\partial x_i}\frac{\partial d}{\partial x_r}\sigma_{x_i}\sigma_{x_r} + 2r(y_i, y_r)\frac{\partial d}{\partial y_i}\frac{\partial d}{\partial y_r}\sigma_{y_i}\sigma_{y_r} + 2r(z_i, z_r)\frac{\partial d}{\partial z_i}\frac{\partial d}{\partial z_r}\sigma_{z_i}\sigma_{z_r} \\ &= -2\left(\frac{\partial d}{\partial x_i}\sigma_{x_i}\right)^2 - 2\left(\frac{\partial d}{\partial y_i}\sigma_{y_i}\right)^2 - 2\left(\frac{\partial d}{\partial z_i}\sigma_{z_i}\right)^2 \end{aligned} \tag{S44}$$

Thanks to the correlation between $\mathbf{x_i}$ and $\mathbf{x_r}$, it appears by combining Equations S43 and S44 that the uncertainty on d theoretically tends to be null. However, although ray tracing establishes that each pixel of the sensor corresponds to one position $\mathbf{x}$ on the sample, in practice it actually images an area around this position that depends on the pixel size s_p. The maximum uncertainty on d is obtained when the illumination spot falls on a corner of the pixel corresponding to $\mathbf{x_i}$ and the observation point on the opposite corner of the pixel corresponding to $\mathbf{x_r}$. On the sensor, it corresponds to an uncertainty of $\sigma_{d_s} = \sqrt{2}s_p = 7.56$ µm. In world space, while taking into account the magnification $m = 0.073$, it follows that $\sigma_d = \frac{\sigma_{d_s}}{m} = 104$ µm.

Angular uncertainties: For one measurement geometry, the illumination direction $\mathbf{w_i}(\theta_i, \phi_i)$ (respectively observation direction $\mathbf{w_r}(\theta_r, \phi_r)$) depends on the camera position $\mathbf{P}$ and the illumination spot $\mathbf{x_i}$ (respectively the observation point $\mathbf{x_r}$):

$$\mathbf{w} = \frac{\mathbf{x} - \mathbf{P}}{\|\mathbf{x} - \mathbf{P}\|} \tag{S45}$$

The associated uncertainty is computed using Equation S7, with $\sigma_P = 44.7$ µm according to the camera model, and σ_{x_i} previously defined in S41.

The angular parameters are defined according to the following equations:

$$\begin{cases} \theta = \arccos(w_z) \\ \phi = \text{atan2}(w_x, w_y) \end{cases} \tag{S46}$$

The uncertainties associated with these parameters are obtained by propagating the uncertainty on $\mathbf{w}$ (cf. Eq. S45) through Equation S46.

Ideally, the position of the illumination spot $\mathbf{x_i}$ on the sample is always the same whatever the measurement geometry is. However, because of optical misalignment, it slightly varies with the configuration of the motorized rotation stages. We define as the illumination angular uncertainties $(\sigma_{\theta_i}, \sigma_{\phi_i})$ the maximum of the uncertainties obtained over all the measurement geometries.

In addition to the small variations due to misalignment, several observation positions $\mathbf{x_r}$ are obtained by measurement geometry, for each pixel imaging the sample. We define as the observation angular uncertainties $(\sigma_{\theta_r}, \sigma_{\phi_r})$ the maximum of the uncertainties obtained over all the measurement geometries and over all the imaging pixels.

We find that for any measurement configuration, $\sigma_\theta \leq 0.05°$ and $\sigma_\phi \leq 2°$.

2. MEASUREMENT PROCESS

In the following, we provide more details about the BSSxDF measurement procedure. Although the process is fully automated, it requires a set of user parameters. It first includes the measurement configurations naming the measurement geometries $(\theta_i, \phi_i, \theta_o, (\phi_o))$ as well as the central wavelengths λ_0 of the spectral illumination of interest. This allows to determine the correct positions of the motorized stages during the acquisition. The camera parameters are also given, including a set of exposure times t_e and an optional averaging factor N corresponding to the number of pictures to capture at each exposure time.

The measurement process is then divided into two parts: the acquisition and the data processing. During acquisition, N pictures are captured per exposure, per illumination, and per measurement geometry. The processing of the data converts the acquired images into numpy binary files containing the BSSxDF data along with the uncertainties. For every acquired picture, the value of every pixel that is considered as valid (cf. Sec. 6.3. of the main paper) is converted into radiance (cf. Eq. 5 of the main paper), then BSSxDF (cf. Eqs. 1. and 2. of the main paper). For one measurement geometry and one spectral illumination, a pixel of coordinates (i, j) can be defined as valid (i.e., well exposed and in focus) for different exposures. Therefore multiple

radiance values are computed for the same observation direction and location on the sample. The measured radiance at this pixel is then defined as the average of the multiple radiance values over the number of exposures for which the pixel is valid, and over the number of measurement repetitions at these exposures. Since pixels are processed independently, no debayering algorithm is applied. For each RGB channel, we use the corresponding calibrated camera response curve.

The full measurement scheme is illustrated in Figure S9.

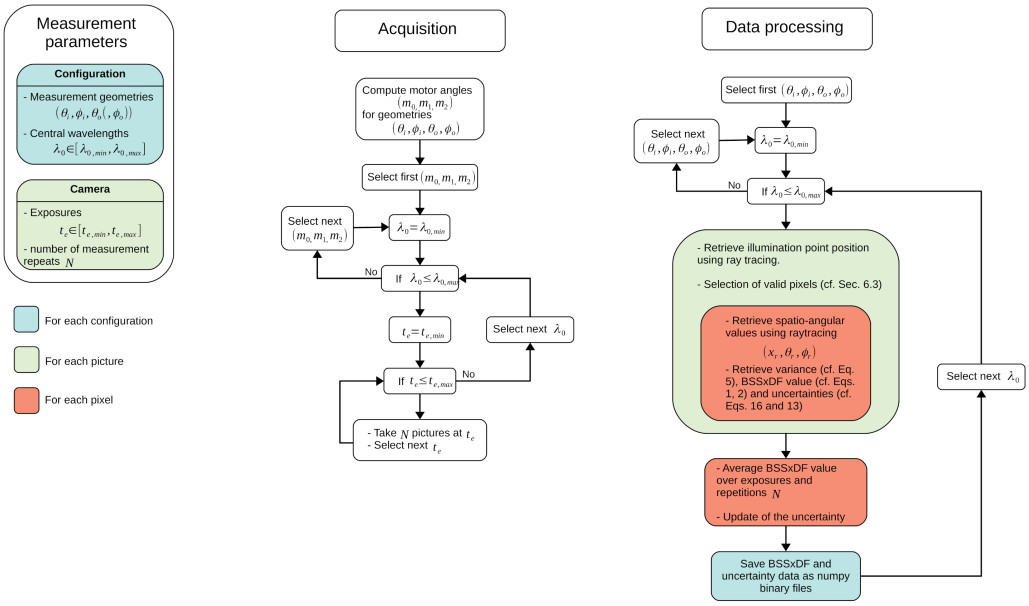

(a) (b) (c)

Fig. S9. Details of the measurement process (cf. Sec. 6.3. and Fig. 11. of the main paper). (a) The user provide the measurement parameters including the configuration parameters (measurement geometries and spectral interval of interest), and the camera parameters (exposure times of interest and optional averaging factor which corresponds to the number of pictures to capture at every exposure time). (b) The acquisition process is fully automatic. For each defined measurement configuration, pictures at various exposures are taken. (c) The processing of the data converts the pictures from the acquisition to binary BSSxDF data files that require much less storage capacity.

3. MEASUREMENT RESULTS

In this section we provide more visualizations of the BSSxDF results obtained on the alabaster sample. We discuss in plane profiles in both reflection and transmission, as well as the angular distribution of the measurements.

A. BSSxDF profiles

The BSSRDF and BSSTDF profiles in Figures S10 and S11 show the dependency on the distance $d_r = |\mathbf{x_i} - \mathbf{x_r}|$ and $d_t = |\mathbf{x_{i,\perp}} - \mathbf{x_t}|$ in the incident plane, where $\mathbf{x_i}$ is the position of the illumination spot on the front face in reflection, and its projection on the sample's back face in transmission.

This visualization demonstrates the importance of spectral measurements: although the alabaster sample appears whitish under ambient light, its measurement under different illuminations show great variations.

The heterogeneity of the sample results in slight variations on the profile values that are systematic whatever the wavelength of interest (specific feature at $d = -7$ mm in reflection or at $d = 17$ mm in transmission for example). In transmission, a slight shift in d of these features with the measurement are noticeable. This attest that the repositioning of the mesh through triangulation and rigid transformation is limited at grazier angles and requires to be improved.

According to Table S1, the BSSRDF relative uncertainty lies between 10% and 20% for any measurement configuration. Higher uncertainties are obtained for observation point close to the illumination spot, due to the possible saturation of the sensor. Otherwise, it is mainly dominated by the uncertainty of the incident flux, and more precisely by the contribution of the integrating sphere albedo ρ.

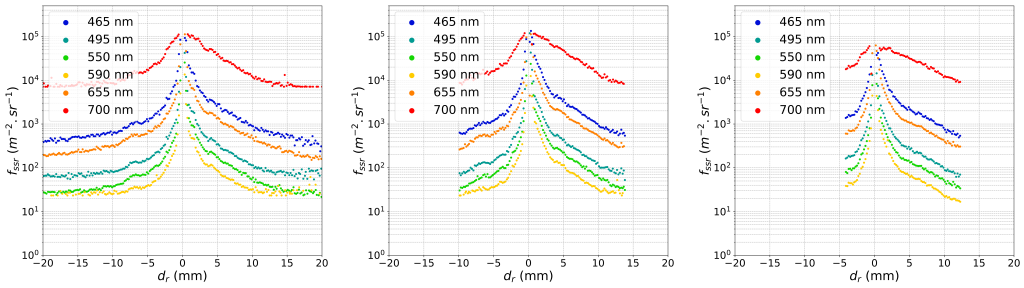

(a) $\theta_o = 20°, \phi_o = 25°$ (b) $\theta_o = 40°, \phi_o = 10°$ (c) $\theta_o = 60°, \phi_o = 5°$

Fig. S10. BSSRDF profiles for incidence $\theta_i = 10°, \phi_i = 60°$, and for different observation directions θ_o. Because our design with three rotation stages only allows for three degrees of freedom, the azimuthal directions ϕ_o are constrained. The grazier the observation direction, the more asymmetric are the profile. The smaller number of plotted data for larger observation angles is due to the smaller number of pixels that are in the focusing range of the camera at these angles. As a consequence, point that are further away from the impact point $\mathbf{x_i}$ are not processed.

λ_0 (nm)	$(\theta_o, \phi_o) = (20°, 25°)$	$(\theta_o, \phi_o) = (40°, 10°)$	$(\theta_o, \phi_o) = (60°, 5°)$
465	0.15	0.14	0.14
495	0.11	0.2	0.1
550	0.1	0.1	0.1
590	0.11	0.11	0.11
655	0.11	0.2	0.16
700	0.16	0.17	0.17

Table S1. Per spectral interval maximum BSSRDF relative uncertainty obtained for profiles at incidence $\theta_i = 10°, \phi_i = 60°$, (cf. Fig. S10). Uncertainties tend to be larger for smaller $d = |\mathbf{x_i} - \mathbf{x_r}|$.

B. BSSxDF angular distributions

The visualization of the measurement angular distribution (θ_r, $\Delta\phi = |\phi_i - \phi_r|$) (respectively ($\theta_t$, $\Delta\phi = |\phi_i - \phi_t|$)) allows to establish how well the reflective (resp. the transmittive) hemisphere is covered, for a given distance $d_r = |\mathbf{x_i} - \mathbf{x_r}|$ (resp. $d_t = |\mathbf{x_{i,\perp}} - \mathbf{x_t}|$) from the illumination spot (cf. Fig. S12). Because of the ambiguity on ϕ_i at normal incidence, only nearly in plane measurements can be performed. The missing geometries in the incident plane are explained by the fact that our design does not allow for back scattering to be measured. For incidences $\theta_i \neq 0°$, out of plane geometries are reached. The grazier the incident angle, the less uniformly sampled is the observation domain.

The observation geometries also depend on the distance to the illumination spot that is considered (cf. Fig. S13). For smaller distances, only directions closed to the camera direction (θ_o, ϕ_o) are actually measured. The corresponding pixels are mostly in the focusing range of the camera, therefore there is a high density of measurement at these geometries. For larger d, the number of

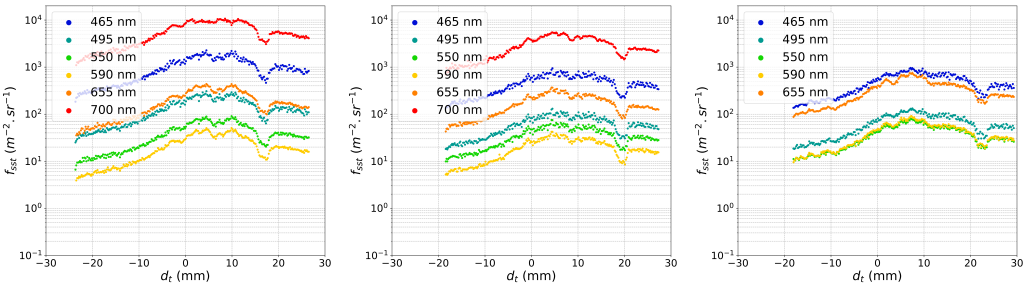

(a) $\theta_o = 200°$, $\phi_o = 335°$ (b) $\theta_o = 210°$, $\phi_o = 345°$ (c) $\theta_o = 220°$, $\phi_o = 350°$

Fig. S11. BSSTDF profiles for incidence $\theta_i = 10°$, $\phi_i = 60°$, and for different observation directions θ_o. Because our design with three rotation stages only allows for three degrees of freedom, the azimuthal directions ϕ_o are constrained. It appears that at grazing angles, characterstic features of the profiles are shifted in d (local minimum at $d = 17$ mm in (a) and at $d = 22$ mm in (c)). This testifies that the repositioning of the mesh through triangulation and rigid transformation is limited at grazier geometries.

in focus pixels decreases therefore fewer measurements are obtained. However, a these are more dispersed across the hemisphere, offering a wider range of observation geometries.

REFERENCES

1. I. BIPM, I. IFCC, I. ISO, and O. IUPAP, "Guide to the expression of uncertainty in measurement, jcgm 100: 2008, gum 1995 with minor corrections," Int. Organ. for Standardization Geneva ISBN (2008).
2. I. Farrance and R. Frenkel, "Uncertainty of measurement: a review of the rules for calculating uncertainty components through functional relationships," The Clin. Biochem. Rev. **33**, 49 (2012).
3. Labsphere, "8° Hemispherical Reflectance Calibration Certificate," https://terraref.ncsa.illinois.edu/clowder/files/5de554fb4f0cc808be61b522/blob/ (2019).
4. D. B. Goldman, "Vignette and exposure calibration and compensation," IEEE transactions on pattern analysis machine intelligence **32**, 2276–2288 (2010).
5. R. Hartley and A. Zisserman, *Multiple view geometry in computer vision* (Cambridge university press, 2003).
6. R. Halır and J. Flusser, "Numerically stable direct least squares fitting of ellipses," in *Proc. 6th International Conference in Central Europe on Computer Graphics and Visualization. WSCG*, vol. 98 (Citeseer, 1998), pp. 125–132.
7. K. T. McDonald, "Error estimation in fitting of ellipses," Lab note (2014).

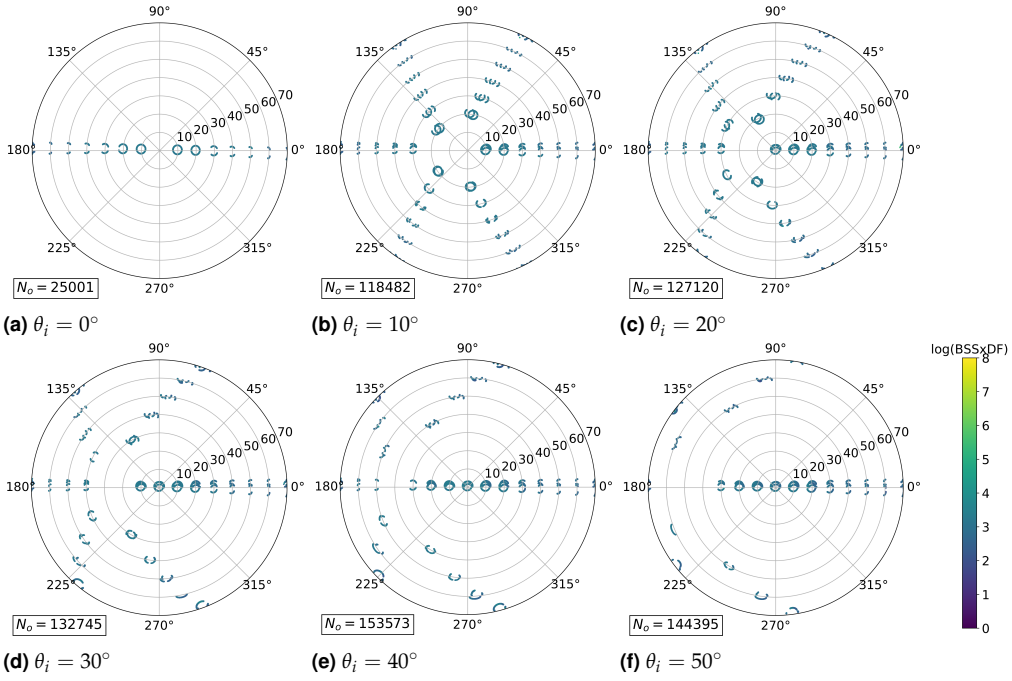

(a) $\theta_i = 0°$ **(b)** $\theta_i = 10°$ **(c)** $\theta_i = 20°$

(d) $\theta_i = 30°$ **(e)** $\theta_i = 40°$ **(f)** $\theta_i = 50°$

Fig. S12. Angular distribution (θ_r, $\Delta\phi = |\phi_i - \phi_r|$) of the measurements performed at 550 nm in reflection on alabaster for a given incidence θ_i and for a given range of distances from the illumination spot $d_r = |x_i - x_r| \in [2, 2.1 \text{ cm}]$. Each plotted point represents one BSSRDF measurement. The total number of valid measurements after data processing is displayed as N_o. Because of the ambiguity on ϕ_i at normal incidence, only nearly in plane measurements can be performed. Out of plane measurements are obtained while increasing the incidence. The grazier the incident angle, the less uniformly sampled is the observation domain.

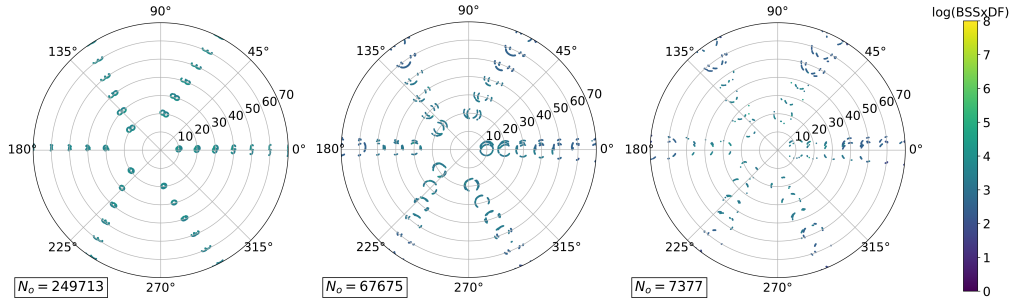

(a) $d \in [1.0, 1.1]\ cm$ **(b)** $d \in [3.0, 3.1]\ cm$ **(c)** $d \in [4.0, 4.1]\ cm$

Fig. S13. Angular distribution (θ_r, $\Delta\phi = |\phi_i - \phi_r|$) of the measurements performed at 550 nm in reflection on alabaster for an incidence $\theta_i = 10°$ and for a different range of distances from the illumination spot $d_r = |x_i - x_r|$. Each plotted point represents one BSSRDF measurement. For observation points that are further away from the illumination spot, there is a higher chance that the corresponding pixels are considered to be out of focus. Therefore the total number of valid measurements after data processing N_o is smaller.